

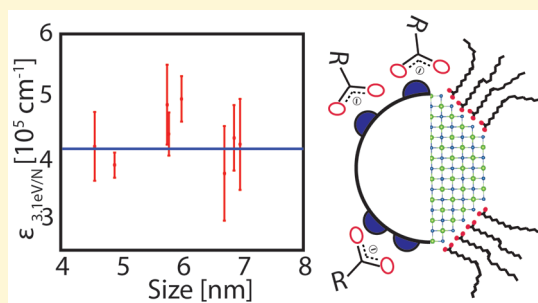
Sizing Curve, Absorption Coefficient, Surface Chemistry, and Aliphatic Chain Structure of PbTe Nanocrystals

Joep L. Peters,¹ Jur de Wit, and Daniël Vanmaekelbergh*¹

Condensed Matter and Interfaces, Debye Institute for Nanomaterials Science, Utrecht University, P.O. Box 80000, 3508 TA Utrecht, The Netherlands

Supporting Information

ABSTRACT: For colloidal semiconductor nanocrystals (NCs), the knowledge of the chemical structure and the size-dependent optical properties is of crucial importance, both from a practical and fundamental perspective. Here, we report the basic properties of PbTe NCs in order to complement the already existing knowledge on PbS and PbSe NCs. The band gap versus NC diameter (sizing) curve was determined by combining transmission electron microscopy with absorption spectroscopy; the energy of the primary optical absorption follows $1/d$ dependence with the diameter. The lead content of the NCs was determined with inductive coupled plasma optical emission spectrometry and the relative tellurium content with energy-dispersive X-ray spectroscopy. Combining these results yields a relation for the intrinsic absorption coefficient, which is independent of the NC size at 3.1 eV. The PbTe NCs are stabilized by Pb(oleate)₂, but different from PbS NCs, oleate is predominantly bound in a chelating bidentate coordination. Besides that, we analyzed the structure of the aliphatic chains on all lead chalcogenide NCs and showed that the aliphatic chains are partly crystalline near the core and more liquid-like at the solvent side.



Colloidal semiconductor nanocrystals (NCs) exhibit size-dependent optoelectronic properties, of interest, for a whole range of applications such as light-emitting devices,¹ field-effect transistors,^{2–4} biomedical imaging,^{5–7} and photo-detectors.^{8,9} PbX (X = S, Se, Te) NCs are of special interest due to their tunable near-IR emission and large exciton Bohr radii.^{10,11} Besides this, PbX NCs have been used as building blocks for several superstructures made by NC assembly, followed by oriented attachment.^{3,12–14} PbX NCs have a rock salt crystal structure; attachment occurs exclusively via (100) facets on which the oleate capping is less strongly bound.¹⁵ Two-dimensional superstructures with several periodic motifs such as the square and honeycomb have been obtained; interestingly, they can all be considered as 2D plane cutouts from a simple cubic lattice.^{14,16}

Because of the low effective mass of the electrons in PbTe, the quantum coupling between attached NCs is even stronger than for the cases of PbS and PbSe.¹⁷ For superstructures of PbTe, novel electronic band structures can be expected, especially for the honeycomb geometry. Furthermore, because of the large mass of Pb and Te, the spin–orbit coupling is strong; PbTe superstructures thus hold promise for future spintronics.¹⁸ In addition, once a PbTe superstructure is fabricated, the Pb²⁺ ion can be exchanged for Cd²⁺ and possibly Hg²⁺.¹⁵ This can result in two-dimensional zinc blende geometric materials with exciting optoelectronics. For example; honeycomb superstructures composed of HgTe are predicted to show the quantum spin Hall effect almost up to room temperature.¹⁹ PbTe is also particularly promising for energy conversion in high-ZT thermoelectric devices.^{20–23}

Control of the nanogeometry is of crucial importance for these thermoelectric devices because the efficiency can be improved by promoting phonon scattering at crystal interfaces or nano-inclusions.^{24,25} Hence, superstructures of PbTe NCs, fabricated in a bottom-up approach, can possibly result in cheap and well-defined materials for thermoelectrics.

Despite these prospects, colloidal PbTe NCs have been far less studied than the PbS and PbSe NC systems. This is due to the problematic chemistry, such as the low synthetic yield and extreme vulnerability to oxygen. Proper chemical synthesis and surface chemistry remains challenging even under the quasi-inert conditions in a glovebox.²⁶ Other difficulties are the discrepancy in the relation between the absorption peak and the NC size^{2,27} and the absence of a way to determine the NC concentration. Furthermore, it has never been examined how (oleate) ligands bind to the PbTe facets, and how the ligand layer is structured; these topics are important to understand issues such as chemical (in)stability, shell-epitaxy, and PbTe NC self-assembly.

Here, we present experiments that resulted in the relation between the energy of the primary absorption peak and the PbTe NC size. An empirical fit establishes a sizing curve, which follows $1/d$ dependence. With the use of the Lambert–Beer law, we were able to determine the molar absorption coefficient at the band gap and at 3.1 eV. The intrinsic

Received: December 5, 2018

Revised: February 8, 2019

Published: February 8, 2019

absorption coefficient at 3.1 eV is size independent; the optical matrix element is entirely determined by the PbTe unit cells and crystal structure. We also investigated the surface chemistry with proton nuclear magnetic resonance (^1H NMR) and Fourier transform infrared spectroscopy (FT-IR), and compared this with the other PbX NCs. This shows that all PbX are bound by z-type Pb(oleate)₂ ligands. Because of the larger unit cell, the oleate is predominantly bound in a chelating bidentate coordination in PbTe NCs instead of a bridging bidentate coordination for PbS. We also measured the structure of the oleate ligands on suspended PbX NCs and showed that the aliphatic chains are partly crystalline near the NC core, while the liquid-like part sticks into the solvent.

THE PBTE SIZING CURVE

The hot-injection method for the synthesis of PbTe NCs is developed by Murphy et al.²⁷ and Urban et al.² and used here to synthesize PbTe NCs in a diameter range between 3.5 and 7 nm. Control over the NC size was most easily achieved by varying the oleic acid/Pb ratio in the Pb precursor or by changing the growth time after injection. Both a higher oleic acid/Pb ratio and a longer growth time resulted in larger NCs. The high-resolution transmission electron microscopy (HR-TEM) images in Figure 1 show that the quasispherical PbTe

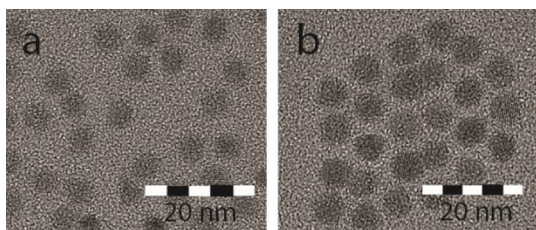


Figure 1. Two HR-TEM images of PbTe NCs of (a) 4.8 and (b) 6.2 nm.

NCs are single-crystalline, without an amorphous layer on the NC surface. To determine the average size of the PbTe NCs in a given batch, approximately 300 particles per batch were analyzed in the same manner for each batch.

Four examples of absorption spectra of the NCs are plotted in Figure 2a, normalized at 400 nm. Although the size dispersion is <10%, the band-edge peak overlaps with other transitions due to its complex band structure. This gives rise to a number of allowed transitions immediately after the first

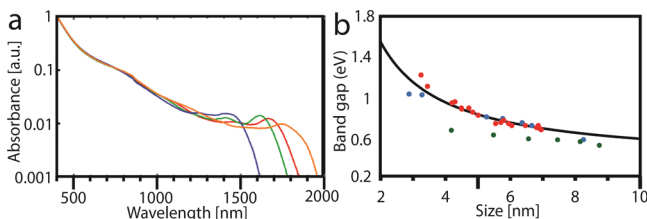


Figure 2. Absorption spectra and the size dependence of the band gap of PbTe NCs. (a) In the logarithmic graph, four absorption spectra of PbTe NCs dissolved in C_2Cl_4 are plotted and normalized at 400 nm. The color coding relates to PbTe NCs with the following sizes: blue 4.9 nm, green 5.7 nm, red 6.0 nm, and orange 6.7 nm. (b) Energy of the first maximum in the absorption, that is, the optical band gap, from this work (red) and previous work, that is, Murphy et al.²⁷ (blue) and Urban et al. (green).²

exciton peak.²⁷ Combining the peak position of the band edge with the NC size determined by transmission electron microscopy (TEM), we could establish a sizing curve as shown in Figure 2b. The red dots are PbTe NCs from this work, while the green dots are from Urban et al.² and the blue dots are of Murphy et al.²⁷ This shows that the data of Urban et al. deviate significantly from the other experimental data. We therefore excluded those data points in the fit for the sizing curve (black line).

The fitted sizing curve for PbTe is

$$E_0 = 0.376 + \frac{1}{0.42d} \quad (1)$$

Here, E_0 is the band gap in eV, and d is the NC diameter in nm. The sizing curve allows us to determine the size of the PbTe NCs immediately from an absorption spectrum, instead of a tedious TEM study. An important factor in this equation is the constant 0.376, which is close to the bulk band gap value of PbTe.^{25,28} Most sizing curves also have a $1/d^2$ term, but its coefficient was too small to contribute in our equation. The predominance of the $1/d$ term was also found experimentally and by calculation for PbSe and PbS NCs.^{29,30} The $1/d$ dependence can be due to a combination of different effects, for example, exciton wave function spill-over, electron–hole many-body effects, and/or deviation from perfect parabolic bands.³¹ The same line of thought can be applied to PbTe, which has a more anisotropic band structure but does have a derivation from parabolicity near the band structure near the band edge.³² The contribution of the $1/d^2$ term might become relevant if a larger NC size range is included. The current synthesis is however not suitable for very small or large NCs. Small NCs are often polydisperse which hinders the size determination, while for larger NCs, a shape change from spherical to quasicubical occurs, which broadens the absorption peak.

QUANTIFYING LIGHT ABSORPTION

We used inductive coupled plasma optical emission spectrometry (ICP–OES) to determine the Pb content in the PbTe NC suspensions investigated. The Pb^{2+} concentrations and their relative standard deviations (RSDs) are shown in Table S1. The sample purity was checked with ^1H NMR (see below). We were unable to reliably measure the Te^{2-} concentration with ICP–OES due to the formation of volatile hydrides. Therefore, we measured the atomic Pb/Te ratios by energy-dispersive X-ray spectroscopy (EDX) shown in Table 1. The total amount of atoms per NC is calculated using eq 2, assuming a spherical shape.

$$N = \frac{4\pi}{3}(d/a)^3 \quad (2)$$

Table 1. Atomic Ratio and Total Number of Atoms per NC for Some PbTe NCs^a

NC size (nm)	Pb atomic (%)	Te atomic (%)	Pb/Te ratio	N (atoms/NC)
4.87	53.87 (0.15)	46.13 (0.10)	1.16	1827
5.74	55.24 (0.42)	44.75 (0.31)	1.24	2992
5.98	54.09 (0.49)	45.90 (0.30)	1.18	3383
6.85	53.59 (1.65)	46.40 (0.95)	1.15	5085

^aThe number between brackets is the RSDs directly from EDX.

where a is the lattice parameter, and d is the particle diameter, both in nm.³³ The amount of atoms is corrected for the uneven Pb/Te ratio, R in eq 3. The number of NCs then follows from the total amount of PbTe unit cells measured in the sample divided by the number of unit cells per NC. Or in other words, the NC concentration C_{NC} is given by

$$C_{\text{NC}} = \frac{1}{N} \frac{(1 + R)}{R} C_{\text{m}} \quad (3)$$

Here, C_{m} is the lead concentration in the sample. We measured an absorption spectrum and combined it with the PbTe NC concentrations to calculate the molar absorption coefficient (also known as molar extinction coefficient) at the band gap, and at 3.1 eV.

■ ABSORPTION COEFFICIENT AT BAND GAP

The band-edge absorption peak is fitted with Gaussian and integrated to get a measure of the NC absorbance of a given sample. From this, the energy-integrated molar absorption coefficient at the band gap ϵ_{gap} is derived using the Lambert–Beer law

$$\log \frac{I}{I_0} = -\epsilon c l = -A \quad (4)$$

where A is the absorbance or absorptivity of our suspension for an optical path length l . A = dimensionless, ϵ = the molar absorption coefficient ($\text{mol}^{-1} \text{cm}^{-1}$), and c denotes the molar concentration of PbTe NCs. Figure 3a presents an overview of

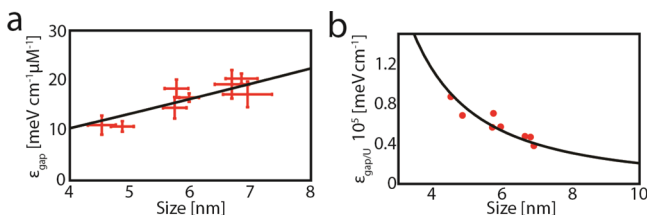


Figure 3. Absorption coefficient of PbTe NCs at the band gap. (a) shows the relation between the energy-integrated molar absorption coefficient at the band gap to the NC size. The horizontal errors account for one standard deviation for the NC size determined by TEM image analysis. The vertical error bar originates from EDX and ICP–OES measurements. (b) Intrinsic energy-integrated absorption coefficient $\epsilon_{\text{gap}/U}$ to the NC size is plotted with an inverse quadratic relation.

the experimental data relating energy-integrated ϵ_{gap} ($\text{meV mol}^{-1} \text{cm}^{-1}$) to NC size. Similar as for PbSe and PbS,³⁰ a power log is used to fit the data. This resulted in the following relation

$$\epsilon_{\text{gap}} = 2.2d^{1.1} \quad (5)$$

The relation obtained from the data is similar compared to the energy-integrated molar absorption coefficients of PbS and PbSe.^{29,30} PbTe NCs, however, absorb less light at the band gap compared to other lead chalcogenides. An additional means of comparison is the energy-integrated absorption coefficient $\epsilon_{\text{gap}/U}$, per unit cell (U), which is calculated with the following formula,³⁰ and shown in Figure 3b

$$\epsilon_{\text{gap}/U} = \frac{6 \ln(10) \epsilon_{\text{gap}}}{\pi d^3 N_{\text{A}}} = 15.5d^{-1.9} \quad (6)$$

This shows that $\epsilon_{\text{gap}/U}$ is size dependent and increases with decreasing size.

■ ABSORPTION COEFFICIENT AT 3.1 EV

We also applied the Lambert–Beer law using the absorption at 3.1 eV. For other NCs, it was found that at this energy, far above the first optical transition, the effects of quantum confinement on the absorption coefficient per unit cell can be neglected.^{29,30,33,34} This would mean that the absorbance per NC should be simply proportional to the number of PbTe unit cells, thus to the NC volume. The experimental results are presented in Figure 4a, which can be fitted with

$$\epsilon_{3.1\text{eV}} = (0.05846 \pm 0.002)d^3 \quad (7)$$

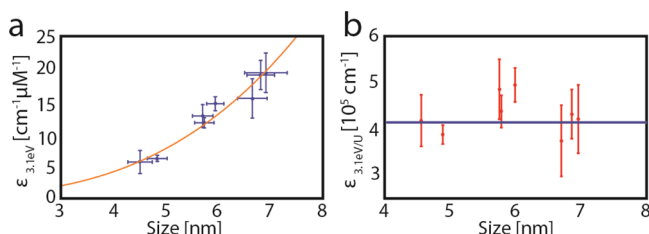


Figure 4. Absorption coefficient of PbTe NCs at 3.1 eV. (a) Molar absorption coefficient at 3.1 eV for different sizes of PbTe NCs. The data points follow d^3 dependence. (b) Intrinsic absorption coefficient $\epsilon_{3.1\text{eV}/U}$ is size independent, as seen from the red dots. The blue line is the calculated $\epsilon_{3.1\text{eV}/U}$ using the bulk PbTe dielectric function.

$\epsilon_{3.1\text{eV}}$ ($\text{cm}^{-1} \text{mol}^{-1}$) can be divided by Avogadro's constant, and the NC volume to yield the intrinsic absorption coefficient (i.e., per PbTe unit cell) is denoted as $\epsilon_{3.1\text{eV}/U}$. This intrinsic absorption coefficient at this energy (sometimes also symbolized by μ) is independent of the NC size (Figure 4b), similar as for other systems.^{29,30,33,34} We note that the absorption coefficient per unit cell at the first transition decreases with increasing size to a value equal to the bulk value.

The size-independent absorption coefficient at $\epsilon_{3.1\text{eV}/U}$ can also be calculated, using the Maxwell–Garnett effective medium theory.^{33,35} For these calculations, the dielectric constant of the solvent tetrachloroethylene³⁶ and the dielectric function of bulk PbTe are needed. The available literature for the dielectric function of bulk PbTe uses tight-binding calculations and band-structure approximations.^{32,37} The most reliable results for the dielectric function and absorption coefficient of PbTe are measured with spectroscopic ellipsometry, which directly measures both real and imaginary components of the dielectric function.³⁸ Based on their data, the local field effect is calculated by the following equation

$$f_{\text{LF}} = \frac{3\epsilon_s}{|\tilde{\epsilon}_{\text{PbTe}} + 2\epsilon_s|} \quad (8)$$

where $\tilde{\epsilon}$ is the composite dielectric function, and ϵ_s is the dielectric function of the solvent. The calculated intrinsic absorption coefficient can subsequently be calculated with

$$\epsilon_{3.1\text{eV}/U} = \frac{2\pi}{\lambda n_s} \left| f_{\text{LF}} \right|_{\text{PbTe,I}}^2 \epsilon_{\text{PbTe,I}} = \frac{\ln(10)A}{fl} \quad (9)$$

where f is the volume fraction, n_s is the refractive index of the solvent, and $\epsilon_{\text{PbTe,I}}$ is the imaginary part of the dielectric

function of PbTe. The calculated value is added in Figure 4b as a blue line. It shows that the calculated and measured intrinsic absorption coefficients are in good agreement.

SURFACE CHEMISTRY OF PBTE NCS

In the case of PbSe and PbS NCS, the ligands have been investigated with FT-IR and ^1H NMR.^{30,39,40} In Figure 5a, we

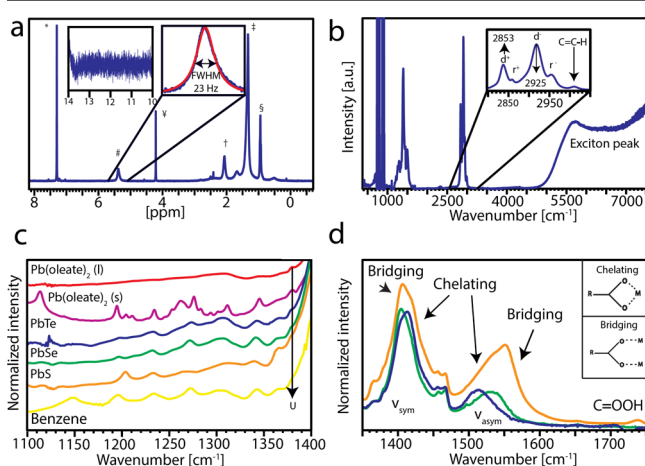


Figure 5. Surface chemistry of PbTe NCS. (a) shows a typical ^1H NMR spectrum of PbTe NCS dissolved in chloroform-*d*, with the left inset showing a zoomed-in image on the region of a possible acid peak and the right inset showing a fit of the vinyl peak, with a full width at half-maximum of 23 Hz. The symbols stand for: * chloroform, # vinyl peak, and ¥ from ferrocene which is added in a known concentration as the internal standard, § methyl group, ‡, and † from other hydrogens in the aliphatic chain. The integral and position of the peaks identifies oleate bound on the NC surface. (b) FT-IR spectrum for PbTe NCS of 7.2 nm in diameter. The saturated bands around 800 and 900 cm^{-1} are from the tetrachloroethylene solvent. The inset shows the CH stretch region with d^+ and d^- , the symmetric and antisymmetric methylene $-\text{CH}_2-$ stretches, and r^+ and r^- , symmetric and antisymmetric methyl $-\text{CH}_3$ stretches. Also, note the clear presence of the $-\text{C}=\text{C}-\text{H}$ stretch. (c) shows FT-IR magnified on the methylene wagging and twisting-rocking progression bands. The graphs are normalized on the CH_2 stretch at 2925 cm^{-1} . The red curve of dissolved $\text{Pb}(\text{oleate})_2$ shows no clear peaks, while clear peaks are visible for solid $\text{Pb}(\text{oleate})_2$ in purple. The blue, green, orange, and yellow graphs are, respectively, PbTe, PbSe, PbS NCS dissolved in tetrachloroethylene (TCE), and PbTe NCS dissolved in benzene. The peaks indicated with U are the methyl symmetric bending (umbrella mode) vibration. (d) shows the carboxylate stretch region, with the symmetric (ν_s) and asymmetric carboxylate (ν_{as}) stretch. The graphs are normalized on the CH_2 stretch at 2925 cm^{-1} . Note that the bands are broad and consist of doublets which are deconvoluted in Figure S2. The underlying peaks are indicative for the type of oleate coordination, either a chelating or bridging bidentate coordination. There is no peak visible at 1710 cm^{-1} showing the absence of oleic acid.

show a typical ^1H NMR spectrum for PbTe NCS dissolved in chloroform-*d*. There are no sharp peaks visible, besides the peaks originating from the solvent molecules, chloroform-*d*, and ferrocene (internal standard). This shows that all other moieties are bound to the NC surface and there are no unreacted precursors in the suspension. The ^1H NMR peak positions and integrals correspond to oleate on the NC surface, which is also confirmed by the absence of an acid peak (left inset Figure 5a).

A typical FT-IR spectrum of PbTe NCS is shown in Figure 5b and also confirms the presence of oleates as major species on the PbTe NC surface. The two saturated peaks around 800 and 900 cm^{-1} originate from the tetrachloroethylene solvent. The inset of Figure 5b shows the CH stretch region, which matches with oleate ligands.³⁹ There are no other broad or sharp peaks, which show the absence of hydroxide or water as a major component on the PbTe NC surfaces, similar as found for PbSe.³⁹ Figure 5d shows a higher magnification on the carboxylic region, where there is no acid peak visible around 1710 cm^{-1} . This confirms that it is oleate that is bound to the NC surface, not oleic acid.

PbTe NCS are dissolved in an apolar solvent, so this would suggest that the negatively charged oleate needs to be charge compensated by positively charged lead atoms. This is confirmed by our EDX analysis in Table 1 showing an excess of Pb^{2+} ions compared to Se^{2-} ; the excess of Pb^{2+} ions on PbTe NCS is similar to that reported for PbS and PbSe NCS.^{29,30} This strongly suggests that the PbTe NCS are capped by $\text{Pb}(\text{oleate})_2$ as z-type ligands, with oleate charge compensated by excess lead.

The ligand density of several samples was determined with either ^1H NMR by the use of an internal standard or FT-IR by the use of a calibration curve.^{39,41,42} This resulted in similar values as found for other semiconductor NCS,^{39,40} ranging from 2.2 to 4.6 oleate/ nm^2 .

OLEATE COORDINATION

The carboxylic vibrations for all three PbX NCS are shown in Figure 5d, normalized on the CH_2 stretching vibration at 2925 cm^{-1} . This shows remarkable differences in the intensities and positions of the symmetric (ν_{sym}) and asymmetric (ν_{asym}) stretch vibrations for the three types of Pb-chalcogenide NCS. We want to remark that the ligand density can alter the carboxylic coordination, but the effects seen here are stronger.³⁹ Also, the NC size and solvent does not influence the coordination significantly (Figures S1 and S2). This means that the results should be related to differences between PbS, PbSe, and PbTe cores.

The energy difference between the symmetric and asymmetric carboxylate stretch is often used to assign the carboxylic bonding coordination.^{43–45} There is however quite some discussion regarding the generality of this method.⁴⁶ Recently, it has been shown by a combination of FT-IR and structural information that similar band positions, as displayed, in Figure 5d, can be attributed to bidentate bridging and chelating coordinations^{47,48} because a monodentate coordination has a higher $\Delta\nu$.⁴⁶ The broadening and non-Lorentzian shape of the bands shown here indicate that both types of carboxylic coordination are present on all PbX surfaces. In Figure S3 and Table S2, we deconvoluted ν_{sym} and ν_{asym} by fitting two Lorentzians under each ν_{sym} and ν_{asym} to separate the different components. Cass et al. found that the low wavelength peak of the ν_{sym} vibration and the high wavelength peak ν_{asym} belong to the bridging bidentate carboxylic coordination,⁴³ while the high wavelength peak of ν_{sym} and the low wavelength peak of ν_{asym} belong to the chelating coordination (see Figure 5d). The assignment was, among other things, based on the observation that the intensity of the coupled peaks vary simultaneously. This seems also to be true for our PbX NCS; the chelating combination has a higher intensity for PbTe (and PbSe NCS), while the bridging peaks are more intense for PbS. The energy difference also matches

the assignment of the coordination because a chelating bidentate coordination generally has a lower $\Delta\nu$ than a bridging bidentate coordination. The energy difference for the chelating bidentate coordination of all three PbX ranges from 90 to 97 cm^{-1} , while it ranges from 131 to 151 cm^{-1} for the bridging bidentate coordination. The intensities of the bands for PbX NCs suggest that the amount of bridging coordinations decreases going from S and Se to Te. It should be noted that it is expected that there is some variations in the peak position and intensity of ν_{sym} and ν_{asym} for different PbX NCs due to differences in the lead carboxylate bonding angle and variation in the Pb–O bond distance.^{44,47,49}

The dominant chelating bidentate coordination for PbTe NCs can be reasoned by the larger unit cell size. The Pb density on the (111) facet of the rock salt PbX crystal, which binds most of the oleate ligands,³⁹ is 6.55, 6.15, and 5.53 nm^{-2} , for PbS, PbSe, and PbTe, respectively. The lead atoms on the (111) facets are partly integrated into the crystal lattice,³⁹ which means that one exposed lead atom on the (111) facet should be charge compensated by one oleate. The density of aliphatic chains is however sterically limited to approximately 4–4.6 chains nm^{-2} on planar surfaces.^{50,51} This means that in the case of PbS, there are much more lead atoms compared to carboxylate groups, meaning that some lead atoms might “share” one carboxylate, resulting in a bridging coordination. Similarly, it was recently found that the Pb–Pb distance in crystalline metal soaps is 4.45 Å. This crystal contained a combination of bridging and chelating bidentate coordinations.⁴⁷ The Pb–Pb distance on the (111) facets in PbS, PbSe, and PbTe is, respectively, 4.20, 4.33 and 4.57 Å, which shows that the likelihood for bridging coordinations is the highest for PbS.

■ ALIPHATIC CHAIN STRUCTURE IN SOLUTION

FT-IR also provides structural information about the aliphatic part of the oleate ligands on the NC surface. The most important feature is the progression of bands between 1150 and 1400 cm^{-1} , which shows a series of well-defined peaks for all-trans crystalline chains and can be assigned to the twisting–rocking and wagging CH_2 vibration.^{52,53} The CH_2 groups in a liquid-like state can move freely, resulting in a large number of rotational isomers which smears the peaks out, and eventually even disappear for liquid chains.^{52,53} This is clearly visible when you compare dissolved $\text{Pb}(\text{oleate})_2$ and solid $\text{Pb}(\text{oleate})_2$ in Figure 5c. The only peak which is still recognizable in the dissolved $\text{Pb}(\text{oleate})_2$ spectrum is the umbrella mode of CH_3 (indicated with a U), which does not depend on chain packing.

The progression bands of solid $\text{Pb}(\text{oleate})_2$ show much resemblance with progression bands recently resolved for the crystalline aliphatic chain of $\text{Zn}(\text{oleate})_2$.⁵⁴ These authors showed that in comparison with $\text{Zn}(\text{stearate})_2$, the hydrocarbon chain before and after the double bond melts independently and therefore has a rather complicated peak pattern.⁵⁴ Recently, Martínez-Casado et al. identified all phase transitions of several saturated lead(II) soaps.⁴⁷ The hydrocarbon chain packing changes from a completely crystalline phase to a rotator phase in which the alkyl chains have rotational freedom. The phase can change further to a liquid crystal before it completely melts to a stable isotropic liquid.⁴⁷ Research on gold and silver NCs showed that the saturated aliphatic chains are partly crystalline; the chains pack in an all-trans conformation near the NC core, while the chains are more liquid-like at the end of the chain.^{55–60} Another

indication of a partially crystalline phase is the exact peak position of the CH_2 stretch vibration. The exact peak positions of the symmetric and asymmetric CH_2 stretch vibration for the crystalline chain are 2850 and 2920 cm^{-1} , respectively. Because of the presence of gauche disorder in the alkyl chain, these peaks shift to higher frequencies for the rotator phase, namely, 2856 and 2928 cm^{-1} .⁴⁷ We found a frequency in the range of 2852–2854 and 2924–2926 cm^{-1} for PbX NCs larger than approximately 4 nm. More freedom of movement at the end of the chain can be seen from the absence of peak splitting of the methyl (CH_3) group at 2957 cm^{-1} (r^- , inset Figure 5b). This points to aliphatic chains that are neither fully crystalline nor fully liquid-like. Because of the different melting behaviors of the aliphatic chain before and after the double bond of oleate,⁵⁴ it is tempting to suggest a predominantly liquid-like phase outward from the double bond to the methyl group and a more crystalline phase inward from the double bond to the NC core.

■ ALIPHATIC CHAIN STRUCTURE IN DIFFERENT SOLVENTS

NCs which are dissolved in benzene show an even more pronounced sequence of peaks, indicating a more solid-like ligand shell (see Figure 5c). The energy difference between the six peaks is approximately equal, suggesting that the complete chain from the core to the double bond is in a solid-like state. Recently, it was found that a broader peak in ^1H NMR indicates less solvated ligands.⁶¹ The peak width of 5.1 nm PbSe NCs dissolved in different solvents confirms this trend. The ^1H NMR spectra are shown in Figure S4, and a comparison of the vinyl peak width is shown in Table 2.

Table 2. Peak Width of the Vinyl Peak in the ^1H NMR Spectra of Oleate-Capped 5.1 nm PbSe NCs

	vinyl peak width [Hz]
chloroform- <i>d</i>	23
hexane- <i>d</i> ₁₄	30
benzene- <i>d</i> ₆	54
toluene- <i>d</i> ₈	56
chlorobenzene- <i>d</i> ₅	47

There is more broadening of the peaks when NCs are dissolved in an aromatic solvent, compared to the smaller tetrachloroethylene and hexane. This indicates that the aromatic solvent molecules are too large to penetrate deeply into the ligand chain, which results in a more solid-like ligand shell. Similar as found before, also halocarbons seem to penetrate deeper into the ligand corona compared to hydrocarbons.⁶²

These findings not only contribute to a better understanding of ligand–ligand interaction in a capping layer but also of the interaction between NCs during self-assembly. Recently, it was shown that these interactions have a large influence on the NC nucleation and growth,⁶³ solubility,^{64,65} and self-assembly.^{62,66–68}

■ CONCLUSIONS

Unlike for PbS and PbSe NCs, a number of basic properties of PbTe NCs were not investigated so far. Above, we reported some crucial optical, chemical, and structural characteristics of state-of-the-art PbTe NCs. First, we established the size dependency of the band gap, demonstrating strong quantum

confinement. We also determined the relation between an absorption spectrum and the PbTe NC concentration. This was done by using the integrated absorbance of the band-edge peak and the absorption at 3.1 eV. The absorbance per PbTe unit cell is size independent at high energy and equal to the bulk value. Next, we compared the surface chemistry of all three types of Pb-chalcogenide NCs. This shows that for common synthesis procedures of PbX NCs, Pb(oleate)₂ is the primary z-type ligand. The binding coordination of the oleate is a combination of bridging and chelating bidentate coordination. Because of limited space on the NCs surface, PbS has the most bridging configurations, while PbTe has the least. Last, we also address the aliphatic chain structure of these oleate ligands on the PbX NCs. This shows that part of the ligand shell closest to the surface is crystalline, while further away from the surface, the ligands are organized in a more liquid-like fashion.

■ EXPERIMENTAL SECTION

Chemicals. 1-Butanol (anhydrous) (99.8%), 1-octadecene (90%), acetonitrile (anhydrous) (99.8%), cadmium(II) acetate dihydrate ($\geq 99.99\%$), cadmium(II) oxide ($\geq 99.99\%$), *n*-chloroform (99.8%), diphenyl ether (99%), ethanol (anhydrous) (99.8%), hexane (anhydrous) (95%), lead acetate trihydrate ($\geq 99.99\%$), methanol (anhydrous) (99.8%), oleic acid (90%), tellurium (325 or 200 mesh) (99.99%), tetrachloroethylene (99.999%), toluene (anhydrous) (99.8%), and trioctylphosphine (TOP; 97%), were all purchased from Sigma-Aldrich and used without purification.

PbTe synthesis was performed based on the method of Urban et al.² The Pb precursor was synthesized in a fumehood by the addition of 1.138 g lead acetate trihydrate (Pb(Ac)₂·3H₂O), 3.3 mL of oleic acid, and 8 mL of octadecene in a three-neck flask. The three-neck flask was put under vacuum in a Schlenk line and flushed with nitrogen (N₂) in order to get rid of O₂ in the reaction atmosphere. This cycle was repeated at least three times. After flushing, the mixture was put under vacuum again, and the temperature was slowly increased to 130 °C. Solid Pb(Ac)₂·3H₂O reacts with oleic acid resulting in the evaporation of acetate and water. The temperature was maintained at 130 °C for at least 3 h, until no bubbling was visible anymore. The tellurium precursor was completely prepared in the glovebox because of its sensitivity to oxygen. Tellurium (0.194 g) was combined with 3 mL of TOP and stirred at ~90 °C, until the solution was completely transparent and yellow.

The previously prepared Pb-oleate is first heated to 170 °C in a three-necked flask in a Schlenk line, after which TOP-Te is rapidly injected under vigorous stirring. Upon injection, the solution immediately turns black. It is of key importance that the injection happens quickly and without stopping the stirring, in order to avoid concentration gradients in the mixture. After 4 min, the growth process was quenched by quickly injecting 3 mL of hexane into the solution. Further cooling of the reaction was achieved by placing the flask in a water bath or blowing cool air onto the flask. Different sizes can be formed through varying reaction times, injection temperature, and oleic acid/lead ratio.

Once the solution had cooled down to room temperature, the PbTe NCs were washed inside a glovebox. The first step was to add water free ethanol with an approximate ratio of 2/3 to the original volume. If the system turned from oily black to dark gray and flaky, it was sufficiently destabilized and placed in a centrifuge. The precipitate was then separated from the supernatant and redispersed in hexane. This washing cycle was repeated five times for every sample in order to get rid of unwanted reaction products and leftover precursors.

The PbTe NC synthesis was performed under inert conditions in a glovebox, and all other experiments were performed as much as possible under inert conditions. Although a slight oxidation of the PbTe surface cannot be excluded,²⁶ we could not find indications of this in the TEM images and in our large data set on the surface chemistry.

The solid lead oleate was made via the method of Hendricks et al.⁶⁹ In short, lead(II) oxide (10.00 g, 44.8 mmol) and acetonitrile (~20 mL) are added to a 100 mL round-bottom flask. The suspension was stirred while being cooled in an ice bath, after which trifluoroacetic acid (0.7 mL, 8.96 mmol, 0.2 equiv) and trifluoroacetic anhydride (6.2 mL, 44.8 mmol, 1 equiv) were added. After 10 min, the yellow lead oxide dissolved, resulting in a clear and colorless solution that was allowed to warm to room temperature. Oleic acid (25.437 g, 90.05 mmol, 2.01 equiv), isopropanol (~180 mL), and triethylamine (10.246 g, 101.25 mmol, 2.26 equiv) were added in a 500 mL Erlenmeyer flask. The lead trifluoroacetate solution was slowly added to the oleic acid solution while stirring, resulting in the formation of a white precipitate. The mixture was heated to reflux and dissolve the precipitate, after which a clear and colorless solution was obtained. The heat was turned off, and the flask was allowed to cool to room temperature, followed by further cooling in a -20 °C freezer for >2 h. The resulting white powder was isolated by suction filtration using a glass-fritted funnel, and the filtrate was thoroughly washed with methanol (3 × 300 mL). Large pieces were crushed to get a white powder. This was subsequently dried under vacuum for >6 h to get a fluffy white powder.

PbSe NCs used for the comparison were made using a procedure described by Campos et al.⁷⁰ The solid Pb-oleate was used as a Pb precursor, while the selenium precursor (*N*-cyclohexylpyrrolidine-1-carboselenoamide) was prepared by mixing selenium (9.0 mmol), pyrrolidine (9.0 mmol), cyclohexyl isocyanide (9.0 mmol), and 10 mL toluene. This mixture was heated to ~100 °C until a clear solution was obtained. If black solid selenium was still present, additional pyrrolidine and/or cyclohexyl isocyanide was added to make sure that all selenium reacted. The mixture was allowed to cool to room temperature at which the selenourea precipitated. The liquid was decanted, and the obtained white solid was placed under vacuum for 24 h. Subsequently, the solid was redissolved in 10 mL toluene at 100 °C and allowed to cool down. The precipitate was filtered, and the solid was placed under vacuum for another 24 h.

The synthesis of PbSe was performed in a Schlenk line where 1.6 g (2.08 mmol, 1.2 equiv) Pb(oleate)₂ was dissolved in 140 mL hexadecane in a 250 mL three-neck flask. 0.45 g (1.7 mmol, 1 equiv) *N*-cyclohexylpyrrolidine-1-carboselenoamide was dissolved in 8 mL diphenyl ether. Both precursors were heated to 100 °C to yield a clear colorless solution. The selenourea was quickly injected into the Pb(oleate)₂ solution which turned brown in approximately 8 s. After 110 min, the reaction was cooled down with an ice bath and inserted inside the glovebox. 90 mL of *n*-butanol and 60 mL of methanol was added to precipitate the NCs. The mixture was centrifuged, and the black residue was dissolved in 10 mL toluene. This solution was washed three more times with methanol.

Characterization. UV-Vis. A PerkinElmer LAMBDA 950 UV/vis spectrometer was used to conduct absorption measurements in the wavelength range from 300 to 2300 nm. The samples were prepared in the glovebox by drying 5–30 μL of PbTe solution under vacuum. The residue was then redispersed in 3 mL TCE because of the absence of absorption features in the near-infrared.

The information captured in the absorption spectrum was acquired in two different ways. First, in the 300–400 nm wavelength region, the volume-corrected absorption was used for further calculations. The second region is the first exciton peak and is different per sample in terms of the peak position and width.

Fourier Transform Infrared Spectroscopy. FT-IR measurements were performed in Bruker vertex 70. A special air-tight liquid cell was used (International Crystal Laboratories) with a path length of 0.5 mm and two KBr crystals at back and front sides to make it transparent for IR light. Spectra were recorded from 400 to 7500 cm⁻¹, with a KBr beam splitter, a DLaTGS D301 detector, and a mid-IR source. Different solvents were used as indicated in the main text.

TEM and EDX. A Tecnai 20 or a Talos F200X (both 200 keV) electron microscope was used. The latter TEM also has the functionality of EDX.

Inductively Coupled Plasma Optical Emission Spectrometry. The exact concentration of lead in PbTe NCs could be obtained with the

PerkinElmer Optima 8300 Optical Emission Spectrometer. The preparation of the calibration curve between 0 and 1 ppm is based on a multielement solution with known amounts of ion species. This range of 5 dilutions was inserted into ICP–OES first, in order to establish the calibration curve.

Pb could not be measured when incorporated in a NC and therefore needed to be dissolved with the use of aqua regia. The next step was to dilute the samples by addition of 5% HNO₃ solution resulting in a Pb concentration in the region between 0 and 1 ppm. The wavelength chosen for Pb is 283.306 nm.

¹H NMR measurements were performed using Agilent MRF400 equipped with a OneNMR probe and Optima Tune system. Spectra were recorded according to the following parameters: 400 MHz, CDCl₃, 25 °C. The ligand density of PbTe NCs was measured via a slightly modified method.^{40,42} In short, a suspension of a known PbTe NC concentration (measured via FT-IR) of an approximate concentration of approximately 4×10^{-4} M was measured including 10 μL (0.05 M) ferrocene stock solution as the internal standard. The concentration of ligands was determined relatively to the internal standard, by integration of the ferrocene peak (4.14 ppm) and the vinyl peak (5.35 ppm), while normalizing for the amount of H atoms present (10:2). Using the size and concentration (FT-IR), we could determine the oleate density/NC. Measurements of PbTe NCs were performed using a longer relaxation delay (30 s) to allow complete relaxation. For Pb(oleate)₂ Δ = 5.3 (m, 4H, HC=CH), 2.2 (t, 4H, ³J_{HH} = 7.3 Hz, CH₂), 2.0 (m, 8H, CH₂), 1.6 (p, 4H, ³J_{HH} = 7.8 Hz, CH₂), 1.4–1.1 (m, 42H, CH₂), and 0.87 (t, 6H, ³J_{HH} = 6.7 Hz, CH₃).

■ ASSOCIATED CONTENT

● Supporting Information

The Supporting Information is available free of charge on the ACS Publications website at DOI: 10.1021/acs.chemmater.8b05050.

Table of the measured atomic composition, FT-IR spectra of the oleate coordination of different NC sizes and in different solvents, deconvolution of the carboxylic vibrations and the corresponding table, and NMR spectra of NCs dissolved in different solvents (PDF)

■ AUTHOR INFORMATION

Corresponding Author

*E-mail: d.vanmaekelbergh@uu.nl.

ORCID

Joep L. Peters: 0000-0002-3415-648X

Daniël Vanmaekelbergh: 0000-0002-3535-8366

Author Contributions

The manuscript was written through contributions of all the authors. All the authors have given approval to the final version of the manuscript.

Notes

The authors declare no competing financial interest.

■ ACKNOWLEDGMENTS

We want to thank Joen Hermans for the fruitful discussion. D.V. acknowledges support from NOW physics (FOM program 152) and from the ERC grant, grant 692691-FIRST STEP.

■ ABBREVIATIONS

NC, nanocrystal; EDX, energy-dispersive X-ray spectroscopy; TEM, transmission electron microscopy; XPS, X-ray photoelectron spectroscopy; ¹H NMR, proton-nuclear-magnetic resonance; FT-IR, Fourier transform infrared spectroscopy;

ICP–OES, inductive coupled plasma optical emission spectrometry

■ REFERENCES

- (1) Pietryga, J. M.; Park, Y.-S.; Lim, J.; Fidler, A. F.; Bae, W. K.; Brovelli, S.; Klimov, V. I. Spectroscopic and Device Aspects of Nanocrystal Quantum Dots. *Chem. Rev.* **2016**, *116*, 10513–10622.
- (2) Urban, J. J.; Talapin, D. V.; Shevchenko, E. V.; Murray, C. B. Self-Assembly of PbTe Quantum Dots into Nanocrystal Superlattices and Glassy Films. *J. Am. Chem. Soc.* **2006**, *128*, 3248–3255.
- (3) Hanrath, T. Colloidal nanocrystal quantum dot assemblies as artificial solids. *J. Vac. Sci. Technol. A Vacuum, Surfaces, Film.* **2012**, *30*, 030802.
- (4) Alimoradi Jazi, M.; Janssen, V. A. E. C.; Evers, W. H.; Tadjine, A.; Delerue, C.; Siebbeles, L. D. A.; van der Zant, H. S. J.; Houtepen, A. J.; Vanmaekelbergh, D. Transport Properties of a Two-Dimensional PbSe Square Superstructure in an Electrolyte-Gated Transistor. *Nano Lett.* **2017**, *17*, 5238–5243.
- (5) Xia, C.; Meeldijk, J. D.; Gerritsen, H. C.; de Mello Donega, C. Highly Luminescent Water-Dispersible NIR-Emitting Wurtzite CuInS₂/ZnS Core/Shell Colloidal Quantum Dots. *Chem. Mater.* **2017**, *29*, 4940–4951.
- (6) Koole, R.; Van Schooneveld, M. M.; Hilhorst, J.; Castermans, K.; David, P.; Strijkers, G. J.; Donegá, C. D. M.; Vanmaekelbergh, D.; Griffioen, W.; Nicolay, K.; Fayad, Z. A.; Meijerink, A.; Willem, J. M. Paramagnetic Lipid-Coated Silica Nanoparticles with a Fluorescent Quantum Dot Core: A New Contrast Agent Platform for Multimodality Imaging. *Bioconjugate Chem.* **2012**, *19*, 2471–2479.
- (7) Mulder, W. J. M.; Koole, R.; Brandwijk, R. J.; Storm, G.; Chin, P. T. K.; Strijkers, G. J. Quantum Dots with a Paramagnetic Coating as a Bimodal Molecular Imaging Probe. *Nano Lett.* **2006**, *6*, 1–6.
- (8) Deng, Z.; Jeong, K. S.; Guyot-Sionnest, P. Colloidal Quantum Dots Intra-band Photodetectors. *ACS Nano* **2014**, *8*, 11707–11714.
- (9) McDonald, S. A.; Konstantatos, G.; Zhang, S.; Cyr, P. W.; Klem, E. J. D.; Levina, L.; Sargent, E. H. Solution-Processed PbS Quantum Dot Infrared Photodetectors and Photovoltaics. *Nat. Mater.* **2005**, *4*, 138–142.
- (10) Allan, G.; Delerue, C. Role of Impact Ionization in Multiple Exciton Generation in PbSe Nanocrystals. *Phys. Rev. B: Condens. Matter Mater. Phys.* **2006**, *73*, 205423.
- (11) Ma, W.; Luther, J. M.; Zheng, H.; Wu, Y.; Alivisatos, A. P. Photovoltaic Devices Employing Ternary PbS_xSe_{1-x}Nanocrystals. *Nano Lett.* **2009**, *9*, 1699–1703.
- (12) Geuchies, J. J.; van Overbeek, C.; Evers, W. H.; Goris, B.; de Backer, A.; Gantapara, A. P.; Rabouw, F. T.; Hilhorst, J.; Peters, J. L.; Konovalov, O.; Petukhov, A. V.; Dijkstra, M.; Siebbeles, L. D. A.; van Aert, S.; Bals, S.; Vanmaekelbergh, D. In Situ Study of the Formation Mechanism of Two-Dimensional Superlattices from PbSe Nanocrystals. *Nat. Mater.* **2016**, *15*, 1248–1254.
- (13) van Overbeek, C.; Peters, J. L.; van Rossum, S. A. P.; Smits, M.; van Huis, M. A.; Vanmaekelbergh, D. Interfacial Self-Assembly and Oriented Attachment in the Family of PbX (X = S, Se, Te) Nanocrystals. *J. Phys. Chem. C* **2018**, *122*, 12464–12473.
- (14) Peters, J. L.; Altantzis, T.; Lobato, I.; Jazi, M. A.; van Overbeek, C.; Bals, S.; Vanmaekelbergh, D.; Sinai, S. B. Mono- and Multilayer Silicene-Type Honeycomb Lattices by Oriented Attachment of PbSe Nanocrystals: Synthesis, Structural Characterization, and Analysis of the Disorder. *Chem. Mater.* **2018**, *30*, 4831–4837.
- (15) Boneschanscher, M. P.; Evers, W. H.; Geuchies, J. J.; Altantzis, T.; Goris, B.; Rabouw, F. T.; van Rossum, S. A. P.; van der Zant, H. S. J.; Siebbeles, L. D. A.; Van Tendeloo, G.; Swart, I.; Hilhorst, J.; Petukhov, A. V.; Bals, S.; Vanmaekelbergh, D. Long-Range Orientation and Atomic Attachment of Nanocrystals in 2D Honeycomb Superlattices. *Science* **2014**, *344*, 1377–1380.
- (16) Evers, W. H.; Goris, B.; Bals, S.; Casavola, M.; de Graaf, J.; van Roij, R.; Dijkstra, M.; Vanmaekelbergh, D. Low-Dimensional Semiconductor Superlattices Formed by Geometric Control over Nanocrystal Attachment. *Nano Lett.* **2012**, *13*, 2317–2323.

- (17) Kagan, C. R.; Murray, C. B. Charge Transport in Strongly Coupled Quantum Dot Solids. *Nat. Nanotechnol.* **2015**, *10*, 1013–1026.
- (18) Žutić, I.; Fabian, J.; Das Sarma, S. Spintronics: Fundamentals and Applications. *Rev. Mod. Phys.* **2004**, *76*, 323.
- (19) Beugeling, W.; Kalesaki, E.; Niquet, Y.; Vanmaekelbergh, D.; Delerue, C.; Smith, C. M. Topological States in Multi-Orbital HgTe Honeycomb Lattices. *Nat. Commun.* **2015**, *6*, 6316.
- (20) Ibáñez, M.; Zamani, R.; Gorsse, S.; Fan, J.; Ortega, S.; Cadavid, D.; Morante, J. R.; Arbiol, J.; Cabot, A. Core-Shell Nanoparticles As Building Blocks for the Bottom-Up Production of Functional Nanocomposites: PbTe-PbS Thermoelectric Properties. *ACS Nano* **2013**, *7*, 2573–2586.
- (21) Rowe, D. M. *CRC Handbook of Thermoelectrics*; CRC Press LLC: Boca Raton, FL, 1995.
- (22) Harman, T. C.; Taylor, P. J.; Walsh, M. P.; Laforge, B. E. Quantum Dot Superlattice Thermoelectric Materials and Devices. *Science* **2002**, *297*, 2229–2232.
- (23) Heremans, J. P.; Jovic, V.; Toberer, E. S.; Saramat, A.; Kurosaki, K.; Charoenphakdee, A.; Yamanaka, S.; Snyder, G. J. Enhancement of Thermoelectric Efficiency in PbTe by Distortion of the Electronic Density of States. *Science* **2008**, *321*, 554–557.
- (24) Faleev, S. V.; Léonard, F. Theory of Enhancement of Thermoelectric Properties of Materials with Nano-inclusions. *Phys. Rev. B: Condens. Matter Mater. Phys.* **2008**, *77*, 214304.
- (25) Kanatzidis, M. G. Nanostructured Thermoelectrics: The New Paradigm? *Chem. Mater.* **2010**, *22*, 648–659.
- (26) Piveteau, L.; Ong, T.-C.; Rossini, A. J.; Emsley, L.; Copéret, C.; Kovalenko, M. V. Structure of Colloidal Quantum Dots from Dynamic Nuclear Polarization Surface Enhanced NMR Spectroscopy. *J. Am. Chem. Soc.* **2015**, *137*, 13964–13971.
- (27) Murphy, J. E.; Beard, M. C.; Norman, A. G.; Ahrenkiel, S. P.; Johnson, J. C.; Yu, P.; Mičić, O. L.; Ellingson, R. J.; Nozik, A. J. PbTe Colloidal Nanocrystals: Synthesis, Characterization, and Multiple Exciton Generation. *J. Am. Chem. Soc.* **2006**, *128*, 3241–3247.
- (28) Ekuma, C. E.; Singh, D. J.; Moreno, J.; Jarrell, M. Optical Properties of PbTe and PbSe. *Phys. Rev. B: Condens. Matter Mater. Phys.* **2012**, *85*, 085205.
- (29) Moreels, I.; Lambert, K.; De Muynck, D.; Vanhaecke, F.; Poelman, D.; Martins, J. C.; Allan, G.; Hens, Z. Composition and Size-Dependent Extinction Coefficient of Colloidal PbSe Quantum Dots. *Chem. Mater.* **2007**, *19*, 6101–6106.
- (30) Moreels, I.; Lambert, K.; Smeets, D.; De Muynck, D.; Nollet, T.; Martins, J. C.; Vanhaecke, F.; Vantomme, A. Size-Dependent Optical Properties of Colloidal PbS Quantum Dots. *ACS Nano* **2009**, *3*, 3023–3030.
- (31) Allan, G.; Delerue, C. Confinement Effects in PbSe Quantum Wells and Nanocrystals. *Phys. Rev. B: Condens. Matter Mater. Phys.* **2004**, *70*, 245321.
- (32) Tudury, G. E.; Marquezini, M. V.; Ferreira, L. G.; Barbosa, L. C.; Cesar, C. L. Effect of Band Anisotropy on Electronic Structure of PbS, PbSe, and PbTe Quantum Dots. *Phys. Rev. B: Condens. Matter Mater. Phys.* **2000**, *62*, 7357–7364.
- (33) Hens, Z.; Moreels, I. Light Absorption by Colloidal Semiconductor Quantum Dots. *J. Mater. Chem.* **2012**, *22*, 10406.
- (34) Xia, C.; Wu, W.; Yu, T.; Xie, X.; van Oversteeg, C.; Gerritsen, H. C.; de Mello Donega, C. Size-Dependent Band-Gap and Molar Absorption Coefficients of Colloidal CuInS₂ Quantum Dots. *ACS Nano* **2018**, *12*, 8350–8361.
- (35) Garnett, J. C. M. Colours in Metal Glasses and in Metallic Films. *Philos. Trans. R. Soc. London, Ser. A* **1904**, *203*, 385–420.
- (36) Maryott, A. A.; Smith, E. R. *Table of Dielectric Constants of Pure Liquids*; United States Department of Commerce, 1951.
- (37) Svane, A.; Christensen, N. E.; Cardona, M.; Chantis, A. N.; Schilfgaarde, M. Van; Kotani, T. Quasiparticle Self-Consistent GW Calculations for PbS, PbSe, and PbTe: Band Structure and Pressure Coefficients. *Phys. Rev. B: Condens. Matter Mater. Phys.* **2010**, *81*, 245120.
- (38) Suzuki, N.; Adachi, S. Optical Properties of PbTe. *Jpn. J. Appl. Phys.* **1994**, *33*, 193–198.
- (39) Peters, J. L.; van den Bos, K. H. W.; Van Aert, S.; Goris, B.; Bals, S.; Vanmaekelbergh, D. Ligand-Induced Shape Transformation of PbSe Nanocrystals. *Chem. Mater.* **2017**, *29*, 4122–4128.
- (40) Moreels, I.; Fritzing, B.; Martins, J. C.; Hens, Z. Surface Chemistry of Colloidal PbSe Nanocrystals. *J. Am. Chem. Soc.* **2008**, *130*, 15081–15086.
- (41) Choi, J. J.; Bealing, C. R.; Bian, K.; Hughes, K. J.; Zhang, W.; Smilgies, D.-M.; Hennig, R. G.; Engstrom, J. R.; Hanrath, T. Controlling Nanocrystal Superlattice Symmetry and Shape-Anisotropic Interactions through Variable Ligand Surface Coverage. *J. Am. Chem. Soc.* **2011**, *133*, 3131–3138.
- (42) Anderson, N. C.; Hendricks, M. P.; Choi, J. J.; Owen, J. S. Ligand Exchange and the Stoichiometry of Metal Chalcogenide Nanocrystals: Spectroscopic Observation of Facile Metal-Carboxylate Displacement and Binding. *J. Am. Chem. Soc.* **2013**, *135*, 18536–18548.
- (43) Cass, L. C.; Malicki, M.; Weiss, E. A. The Chemical Environments of Oleate Species within Samples of Oleate-Coated PbS Quantum Dots. *Anal. Chem.* **2013**, *85*, 6974–6979.
- (44) Mesubi, M. A. An Infrared Study of Zinc, Cadmium, and Lead Salts of Some Fatty Acids. *J. Mol. Struct.* **1982**, *81*, 61–71.
- (45) Deacon, G.; Phillips, R. J. Relationships between the Carbon-Oxygen Stretching Frequencies of Carboxylate Complexes and the Type of Carboxylate Coordination. *Coord. Chem. Rev.* **1980**, *33*, 227–250.
- (46) Zelenák, V.; Vargová, Z.; Györyová, K. Correlation of infrared spectra of zinc(II) carboxylates with their structures. *Spectrochim. Acta A Mol. Biomol. Spectrosc.* **2007**, *66*, 262–72.
- (47) Martínez-Casado, F. J.; Ramos-Riesco, M.; Rodríguez-Cheda, J. A.; Redondo-Yélamos, M. I.; Garrido, L.; Fernández-Martínez, A.; García-Barriocanal, J.; da Silva, I.; Durán-Olivencia, M.; Poulain, A. Lead(II) Soaps: Crystal Structures, Polymorphism, and Solid and Liquid Mesophases. *Phys. Chem. Chem. Phys.* **2017**, *19*, 17009–17018.
- (48) Ellis, H. A.; White, N. A.; Hassan, I.; Ahmad, R. A room temperature structure for anhydrous lead (II) decanoate. *J. Mol. Struct.* **2002**, *642*, 71–76.
- (49) Catalano, J.; Murphy, A.; Yao, Y.; Yap, G. P. A.; Zumbulyadis, N.; Centeno, S. A.; Dybowski, C. Coordination geometry of lead carboxylates - spectroscopic and crystallographic evidence. *Dalton Trans.* **2015**, *44*, 2340–2347.
- (50) Strong, L.; Whitesides, G. M. Structures of Self-Assembled Monolayer Films of Organosulfur Compounds Adsorbed on Gold Single Crystals: Electron Diffraction Studies. *Langmuir* **1988**, *4*, 546–558.
- (51) Ulman, A. Formation and Structure of Self-Assembled Monolayers. *Chem. Rev.* **1996**, *96*, 1533–1554.
- (52) Maroncelli, M.; Qi, S. P.; Strauss, H. L.; Snyder, R. G. Nonplanar Conformers and the Phase Behavior of Solid N-Alkanes. *J. Am. Chem. Soc.* **1982**, *104*, 6237–6247.
- (53) Snyder, R. G. Vibrational Study of the Chain Conformation of the Liquid n-Paraffins and Molten Polyethylene. *J. Chem. Phys.* **1967**, *47*, 1316–1360.
- (54) Barman, S.; Vasudevan, S. Contrasting Melting Behavior of Zinc Stearate and Zinc Oleate. *J. Phys. Chem. Lett. B* **2006**, *110*, 651–654.
- (55) Hostetler, M. J.; Stokes, J. J.; Murray, R. W.; Hill, C.; Carolina, N. Infrared Spectroscopy of Three-Dimensional Self-Assembled Monolayers: N-Alkanethiolate Monolayers on Gold Cluster Compounds. *Langmuir* **1996**, *12*, 3604–3612.
- (56) Badia, A.; Gao, W.; Singh, S.; Demers, L.; Cuccia, L.; Reven, L. Structure and Chain Dynamics of Alkanethiol-Capped Gold Colloids. *Langmuir* **1996**, *12*, 1262–1269.
- (57) Badia, A.; Cuccia, L.; Demers, L.; Morin, F.; Lennox, R. B. Structure and Dynamics in Alkanethiolate Monolayers Self-Assembled on Gold Nanoparticles: A DSC, FT-IR, and Deuterium NMR Study. *J. Am. Chem. Soc.* **1997**, *119*, 2682–2692.

(58) Hostetler, M. J.; Green, S. J.; Stokes, J. J.; Murray, R. W. Monolayers in Three Dimensions: Synthesis and Electrochemistry of ω -Functionalized Alkanethiolate-Stabilized Gold Cluster Compounds. *J. Am. Chem. Soc.* **1996**, *118*, 4212–4213.

(59) Pradeep, T.; Mitra, S.; Nair, A. S.; Mukhopadhyay, R. Dynamics of Alkyl Chains in Monolayer-Protected Au and Ag Clusters and Silver Thiolates: A Comprehensive Quasielastic Neutron Scattering Investigation. *J. Phys. Chem. B* **2004**, *108*, 7012–7020.

(60) Mukhopadhyay, R.; Mitra, S.; Johnson, M.; Kumar, V. R. R.; Pradeep, T. Evolution of the Alkyl-Chain Dynamics in Monolayer-Protected Gold Clusters. *Phys. Rev. B: Condens. Matter Mater. Phys.* **2007**, *75*, 075414.

(61) De Roo, J.; Yazdani, N.; Drijvers, E.; Lauria, A.; Maes, J.; Owen, J. S.; Van Driessche, I.; Niederberger, M.; Wood, V.; Martins, J. C.; Infante, I.; Hens, Z. Probing Solvent–Ligand Interactions in Colloidal Nanocrystals by the NMR Line Broadening. *Chem. Mater.* **2018**, *30*, 5485–5492.

(62) Wei, J.; Schaeffer, N.; Pileni, M.-P. Solvent-Mediated Crystallization of Nanocrystal 3D Assemblies of Silver Nanocrystals: Unexpected Superlattice Ripening. *Chem. Mater.* **2015**, *28*, 293–302.

(63) Yin, Y.; Alivisatos, A. P. Colloidal nanocrystal synthesis and the organic-inorganic interface. *Nature* **2005**, *437*, 664–670.

(64) Yang, Y.; Qin, H.; Jiang, M.; Lin, L.; Fu, T.; Dai, X.; Zhang, Z.; Niu, Y.; Cao, H.; Jin, Y.; Zhao, F.; Peng, X. Entropic Ligands for Nanocrystals: From Unexpected Solution Properties to Outstanding Processability. *Nano Lett.* **2016**, *16*, 2133–2138.

(65) Yang, Y.; Qin, H.; Peng, X. Intramolecular Entropy and Size-Dependent Solution Properties of Nanocrystal – Ligands Complexes. **2016**, *2131*, 2–7. DOI: [10.1021/acs.nanolett.6b00737](https://doi.org/10.1021/acs.nanolett.6b00737)

(66) Goubet, N.; Richardi, J.; Albouy, P.-A.; Pileni, M.-P. Which Forces Control Supracrystal Nucleation in Organic Media? *Adv. Funct. Mater.* **2011**, *21*, 2693–2704.

(67) Quan, Z.; Xu, H.; Wang, C.; Wen, X.; Wang, Y.; Zhu, J.; Li, R.; Sheehan, C. J.; Wang, Z.; Smilgies, D.-M.; Luo, Z.; Fang, J. Solvent-Mediated Self-Assembly of Nanocube Superlattices. *J. Am. Chem. Soc.* **2014**, *136*, 1352–1359.

(68) Wang, Z.; Bian, K.; Nagaoka, Y.; Fan, H.; Cao, Y. C. Regulating Multiple Variables to Understand the Nucleation and Growth and Transformation of PbS Nanocrystal Superlattices. *J. Am. Chem. Soc.* **2017**, *139*, 14476–14482.

(69) Hendricks, M. P.; Campos, M. P.; Cleveland, G. T.; Jen-La Plante, I.; Owen, J. S. A Tunable Library of Substituted Thiourea Precursors to Metal Sulfide Nanocrystals. *Science* **2015**, *348*, 1226–1230.

(70) Campos, M. P.; Hendricks, M. P.; Beecher, A. N.; Walravens, W.; Swain, R. A.; Cleveland, G. T.; Hens, Z.; Sfeir, M. Y.; Owen, J. S. A Library of Selenourea Precursors to PbSe Nanocrystals with Size Distributions near the Homogeneous Limit. *J. Am. Chem. Soc.* **2017**, *139*, 2296–2305.